

## Durham Research Online

---

### Deposited in DRO:

22 June 2015

### Version of attached file:

Published Version

### Peer-review status of attached file:

Peer-reviewed

### Citation for published item:

Turner, S. and Beier, C. and Niu, Y.L. and Cook, C. (2011) 'U-Th-Ra disequilibria and the extent of off-axis volcanism across the East Pacific Rise at 930N, 1030N, and 1120N.', *Geochemistry, geophysics, geosystems.*, 12 (7). Q0AC12.

### Further information on publisher's website:

<http://dx.doi.org/10.1029/2010GC003403>

### Publisher's copyright statement:

Turner, S., C. Beier, Y. Niu, and C. Cook (2011), U-Th-Ra disequilibria and the extent of off-axis volcanism across the East Pacific Rise at 930N, 1030N, and 1120N, *Geochemistry, Geophysics, Geosystems*, 12, Q0AC12, doi: 10.1029/2010GC003403. To view the published open abstract, go to <http://dx.doi.org> and enter the DOI.

### Additional information:

---

### Use policy

The full-text may be used and/or reproduced, and given to third parties in any format or medium, without prior permission or charge, for personal research or study, educational, or not-for-profit purposes provided that:

- a full bibliographic reference is made to the original source
- a [link](#) is made to the metadata record in DRO
- the full-text is not changed in any way

The full-text must not be sold in any format or medium without the formal permission of the copyright holders.

Please consult the [full DRO policy](#) for further details.



# U-Th-Ra disequilibria and the extent of off-axis volcanism across the East Pacific Rise at 9°30'N, 10°30'N, and 11°20'N

**Simon Turner**

*GEMOC, Department of Earth and Planetary Sciences, Macquarie University, Sydney, New South Wales 2109, Australia (simon.turner@mq.edu.au)*

**Christoph Beier**

*GeoZentrum Nordbayern, Universität Erlangen-Nürnberg, Schoßgarten 5, D-91054 Erlangen, Germany*

**Yaoling Niu**

*Department of Earth Sciences, University of Durham, Science Laboratories, Durham DH1 3LE, UK*

**Craig Cook**

*Science and Engineering, University of Waikato, Hamilton PB3105, New Zealand*

[1] There is widespread interest in the distance that mid-ocean ridge magmatism extends beyond the neovolcanic zone. Off-axis magmas also provide a means to map out variations across the melting zone. We present  $^{238}\text{U}$ - $^{230}\text{Th}$ - $^{226}\text{Ra}$  data for 35 well-characterized samples that extend up to 50 km away from the ridge axis across the East Pacific Rise at 9°30'N, 10°30'N, and 11°20'N. The ( $^{230}\text{Th}/^{238}\text{U}$ ) ratios range from 1.00 to 1.19, and the ( $^{226}\text{Ra}/^{230}\text{Th}$ ) ratios range from 1 to 2.78. The samples have a bimodal ( $^{230}\text{Th}/^{238}\text{U}$ ) distribution with approximately half overlying published axial data on the U-Th diagram and the remainder lying close to the equiline. The U series disequilibria in the majority of the samples can be explained by aging subsequent to eruption in a zone ~8 km wide about the neovolcanic zone, consistent with visual evidence for sample age. Nevertheless, seven of the samples lie above calculated ( $^{230}\text{Th}/^{238}\text{U}$ ) axial decay curves and/or have  $^{226}\text{Ra}$  excesses implying eruption tens of kilometers off axis. These are consistent with evidence from seamounts and seismic interpretations that magmatism can extend up to 20 km off axis. The implication is that magma is not as efficiently focused beneath the ridge axis as has generally been believed. There is a decrease in initial ( $^{230}\text{Th}/^{238}\text{U}$ ) in both these and published samples inferred to have formed off axis, but there is no compelling evidence that this reflects source heterogeneity. Simple modeling suggests that this could be explained by a decrease in fertility and melt column length as the overlying lithosphere thickens with age and the solidus shallows.

**Components:** 11,400 words, 7 figures, 4 tables.

**Keywords:** East Pacific Rise; U-Th-Ra disequilibria; mid-ocean ridge basalt; off-axis magmatism.

**Index Terms:** 1009 Geochemistry: Geochemical modeling (3610, 8410); 1032 Geochemistry: Mid-oceanic ridge processes (3614, 8416); 1037 Geochemistry: Magma genesis and partial melting (3619).

**Received** 18 October 2010; **Revised** 25 March 2011; **Accepted** 29 March 2011; **Published** 28 July 2011.

Turner, S., C. Beier, Y. Niu, and C. Cook (2011), U-Th-Ra disequilibria and the extent of off-axis volcanism across the East Pacific Rise at 9°30'N, 10°30'N, and 11°20'N, *Geochem. Geophys. Geosyst.*, 12, Q0AC12, doi:10.1029/2010GC003403.

**Theme:** Geochemical Heterogeneities in Oceanic Island Basalt and Mid-ocean Ridge Basalt Sources: Implications for Melting Processes and Mantle Dynamics

## 1. Introduction

[2] More than 70% of global volcanism consists of basalts erupted at mid-ocean ridges (MORB) and this is generally thought to be confined to a narrow axial zone [Fornari *et al.*, 2004] and/or efficient magma focusing from a much broader, triangular melting region [e.g., Spiegelman and McKenzie, 1987; Plank and Langmuir, 1992; Korenaga and Kelemen, 1997]. However, the dynamics of melting and melt transport remain a subject of debate. In this regard, U series isotope studies have proved especially useful because of their ability to constrain melting rates and melt extraction porosity (see Elliott and Spiegelman [2003] for a review). One of the most intensively studied of the global ocean ridges is the fast spreading (11.1 cm/yr) East Pacific Rise (EPR) which appears to be underlain by axial magma chambers (see Sinton and Detrick [1992] or Fornari *et al.* [2004] and references therein for a summary). Although U series isotope data have been extensively analyzed from ~ zero-aged, axial EPR samples, analogous to other settings (e.g., arcs) their interpretation is nonunique and open to question. For example, the effects of source compositional the style of melt extraction (such as dynamic melting versus equilibrium porous flow, versus two-porosity models) and the possibility that disequilibria could be created in the crust instead of the mantle remain controversial [e.g., Lundstrom *et al.*, 1999; Jull *et al.*, 2002; Saal and Van Orman, 2004].

[3] How the composition, eruption temperature and supply rate of MORB may vary as a function of time have been studied using samples (lavas) collected along ridge-perpendicular transects across the EPR axis [Perfit *et al.*, 1994; Batiza *et al.*, 1996; Niu *et al.*, 1999; Regelous *et al.*, 1999; Reynolds and Langmuir, 2000]. It is important to note, however, that this approach implicitly assumes that all these samples studied were originally formed in the very narrow (<1–2 km) axial zone. This assumption may be reasonable to a first order but geophysical surveys indicate that the oceanic crust continues to thicken (by a factor of ~2) over several km away from the ridge axis [e.g., Christeson *et al.*, 1992; Harding *et al.*, 1993; Sohn *et al.*, 2004]. This requires the occurrence of magmatism beyond the axis including lavas flows breaching the axial trough and being deposited on the ridge flanks [e.g., Soule *et al.*, 2005]. This inference has been supported by both submersible observation [e.g., Perfit *et al.*, 1994] and U series dating that has yielded ages younger than the spreading age (i.e., that predicted by com-

binning the distance of the sample from the axis with the local spreading rate) [e.g., Goldstein *et al.*, 1994; Rubin *et al.*, 1994]. For example, in the region 9–10°N, Sims *et al.* [2003] used U series data to demonstrate the persistence of volcanism up to 4 km from the ridge axis. More strikingly, Zou *et al.* [2002] presented U-Th isotope evidence for magmatism as far off axis as 20 km at 9°30'N. The latter results were highly controversial, especially the occurrence of several samples with <sup>238</sup>U excesses that are not anticipated in MORB [e.g., Elliott, 2002]. Nevertheless, Durant and Toomey [2009] present seismic evidence for the existence of a melt lens 20 km to the east of the ridge axis and numerical modeling that suggests that bending stresses may open tensile fractures which may accommodate off-axis magmatism out to distances of ~20 km from the axis [Sohn and Sims, 2005].

[4] In order to explore these substantial matters further, we have undertaken U-Th-Ra analyses of samples from traverses across the EPR at 10°30'N and 11°20'N as well as reanalyzing some of the more unusual samples from Zou *et al.* [2002] at 9°30'N. We have also obtained the first <sup>226</sup>Ra data for samples from the three traverses. Our objectives are to (1) see if some of the more unusual results from the Zou *et al.* [2002] data from 9°30'N are correct, (2) conduct a similar experiment along the two other traverses across the EPR, (3) ascertain the frequency and location of any off-axis flows, (4) investigate any contrasts in composition and/or melting dynamics between axial and off-axis MORB, and (5) determine whether the inferred temporal changes in eruption temperature and/or composition for the EPR MORB need reappraisal.

## 2. Sample Locations and Background Data

[5] The samples we analyzed were collected during Phoenix, leg 2 (*R/V Melville*) by dredging and rock coring along flow lines on both the Cocos and Pacific plates out to 40–50 km (or ~800 kyr equivalent spreading age and the Brunhes magnetic reversal) from the ridge axis (Figure 1). They come from three traverses conducted across the EPR axis at 9°30'N, 10°30'N and 11°20'N that were originally conducted in order to investigate temporal changes in axial magma chemistry over the last 800 kyr [Batiza *et al.*, 1996]. All samples collected from the axis appeared extremely fresh in hand specimen (i.e., black and glassy). Samples collected away from the axis appear progressively older with

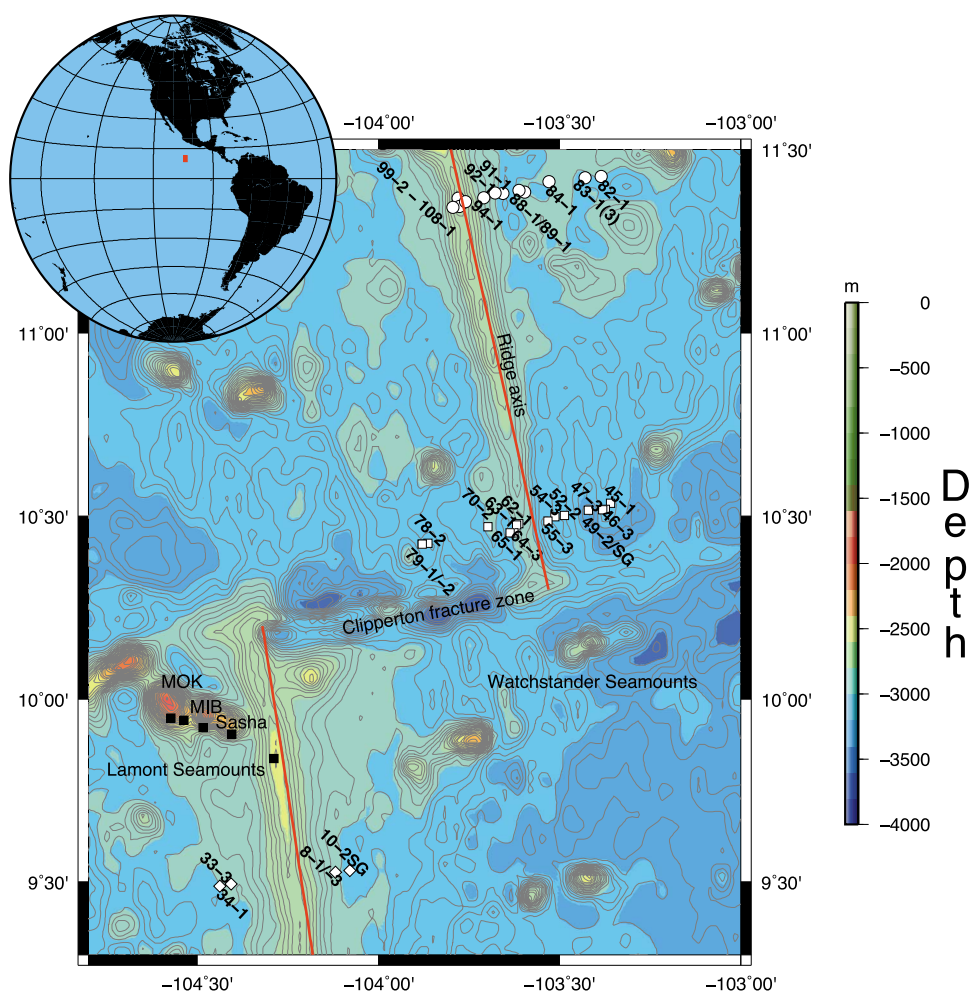


**Figure 1.** Map of the East Pacific Rise using UT [Wessel and Smith, 1991, 1998] showing major transform faults and the three across-ridge traverses with sample localities indicated.

more alteration and thicker Mn coatings as a function of distance away from the EPR axis. The majority of the samples were dredged from small fault scarps [Batiza *et al.*, 1996].

[6] Batiza *et al.* [1996] concluded that both 9°30'N and 11°20'N are magmatically robust ridge segments whereas 10°30'N appears to be a magmatically starved axis. Some major and trace element data for samples from 9°30'N were presented by Batiza *et al.* [1996] and U-Th and Pb isotope data by Zou *et al.* [2002]. Regelous *et al.* [1999] and Niu *et al.* [1999] present major and trace element and Sr-Nd-Pb isotope data for the samples from 10°30'N and 11°20'N, respectively. The samples from 10°30'N are dominated by normal- or N-MORB and show temporal changes in major elements that are not accompanied by systematic changes in trace element or radiogenic isotopes and have been interpreted to reflect changes in eruption tempera-

ture and, by inference, magma supply rate through time [Batiza *et al.*, 1996; Regelous *et al.*, 1999]. In contrast, samples from the traverse at 11°20'N contain a number of enriched- or E-MORB and exhibit significant variation in radiogenic isotopes interpreted to result from mixing with plume-like heterogeneities [Niu *et al.*, 1999].

[7] We chose the four Zou *et al.* [2002] samples from 9°30'N that had the most extreme disequilibria for reanalysis (PH33-3 and PH8-1 with <sup>230</sup>Th excess and PH34-1 and PH10-2 that had <sup>238</sup>U excess), plus a second sample from dredge 8 (sample PH8-3). From 10°30'N we selected 15 samples extending out 31 km from the axis corresponding to spreading rate ages ranging from 8 to 556 kyr. These included 2 samples from dredge 79 (PH79-1 and PH79-2). Along the 11°20'N traverse we selected 15 samples extending out to 48 km with an



associated range in spreading rate ages ranging from 7 to 873 kyr.

### 3. Preparation and Analytical Methods

[8] We used methods employed previously in the Macquarie University U series laboratory for submarine glass samples [Beier *et al.*, 2010]. Suitable glasses were crushed with an agate mortar and pestle to 0.5–1 mm sized chips, washed in deionized water and hand-picked under a binocular microscope to avoid pieces with visible evidence for crystals, vesicles, hydrothermal alteration and/or Mn coatings. Selected glass chips were then ultrasonicated in cold 2.5N HCl and 30% H<sub>2</sub>O<sub>2</sub> (1:1 mix) for 10–20 min before being washed and ultrasonicated (20 min) in deionized water [e.g., Kokfelt *et al.*, 2005; J. Gill, personal communication, 2005]. The glasses were then reinspected for alteration and hand picked again to obtain a 0.2–1 g quantity of clean glass chips. We analyzed U-Th in leachates from 3 samples in order to appraise the effects of the cleaning procedure (<sup>226</sup>Ra concentrations below detection limit).

[9] U, Th and Ra concentrations and isotope ratios were determined on samples and leachates that were spiked with <sup>236</sup>U-<sup>229</sup>Th and <sup>228</sup>Ra tracers. Glass chips were dissolved using an HF-HNO<sub>3</sub>-HCl mix in heated Teflon pressure bombs. All acids were Teflon distilled. The product was converted to chloride using 6N HCl and then 6N HCl saturated with H<sub>3</sub>BO<sub>3</sub> to remove residual fluorides. The final product was then converted to nitrate using 14N HNO<sub>3</sub> and finally taken up in 7N HNO<sub>3</sub>. U and Th purification was achieved via a single pass through a 4 ml anionic resin column using 7N HNO<sub>3</sub>, 6N HCl and 0.2N HNO<sub>3</sub> as eluents. We purposefully avoided the use of EiChrom® resins for the U-Th chemistry as these can bleed organics that lead to memory effects and interferences during MC-ICP-MS analysis. Concentrations and isotope ratios were measured in dynamic mode on a Nu Instruments® MC-ICP-MS at Macquarie University. <sup>238</sup>U and <sup>235</sup>U were analyzed on Faraday cups, using the <sup>238</sup>U/<sup>235</sup>U ratio to determine the U mass bias, assuming <sup>238</sup>U/<sup>235</sup>U = 137.88, while <sup>236</sup>U and <sup>234</sup>U were alternately collected in the IC0 ion counter that is preceded by an energy filter. The IC0 gain was determined during interspersed dynamic analyses of CRM145 assuming a <sup>234</sup>U/<sup>238</sup>U ratio of  $5.286 \times 10^{-5}$  [Cheng *et al.*, 2000]. Methods for Th isotope measurements employed a dynamic routine with <sup>232</sup>Th in Faraday cups and <sup>230</sup>Th and <sup>229</sup>Th alternating on IC0 and using bracketing measurements of

the Th“U” (Open University Th solution) standard to obtain the Th mass bias which can be up to 4‰ different to that for U [e.g., Hoffmann *et al.*, 2007]. Measurements at masses 230.5 and 229.5 were used to derive a linear correction for residual <sup>232</sup>Th tail interference as described in detail for the GEMOC laboratory in Appendix A of Sims *et al.* [2008]. For our setup, a polynomial tail correction can lead to a  $\leq 0.6\%$  lower <sup>230</sup>Th/<sup>232</sup>Th ratio (but see also discussion below). However, there is no a priori reason to assume that the tail has a polynomial form. Typical within run errors on <sup>234</sup>U/<sup>238</sup>U and <sup>230</sup>Th/<sup>232</sup>Th ratio measurements were  $2.61 \times 10^{-8}$  and  $1.10 \times 10^{-8}$ , respectively.

[10] The Ra analysis procedure follows that used by Turner *et al.* [2000]. Ra was taken from the first elution from the anionic column and converted to chloride using 6N HCl. This was then loaded in 3 N HCl onto an 8 ml cationic column and Ra eluted using 3.75M HNO<sub>3</sub> and the process repeated on a scaled-down 0.6 ml column. The REE were then removed using a 150  $\mu$ l column of EiChrom® Ln-spec resin™ and 0.1N HNO<sub>3</sub>. Ra and Ba were finally chromatographically separated using EiChrom® Sr-spec resin™ and 3N HNO<sub>3</sub> as eluent in a 150  $\mu$ l procedure. Samples were loaded onto degassed Re filaments using a Ta-HF-H<sub>3</sub>PO<sub>4</sub> activator solution [Birck, 1986] and <sup>228</sup>Ra/<sup>226</sup>Ra ratios were measured to a precision  $\leq 1\%$  in dynamic ion counting mode on a ThermoFinnigan Triton® TIMS at Macquarie University. Organic interferences are often noted at low temperatures during TIMS analysis for Ra but were eliminated here by using the instrument fitted with a dry scroll pump instead of the standard rotary pump. This prevents leakage of organic molecules into the source during venting.

[11] In order to be able to demonstrate genuine departures from secular equilibrium in the EPR samples it is important to adopt a conservative estimate for analytical precision. Table 1 contains results for a number of equilibrium rock standards that were analyzed over the same 2 year period (2007–2008) as the traverse samples. The analyses of TML-3, BCR-1 and BCR-2 are generally within error of published values and within 2 standard errors of secular equilibrium for (<sup>230</sup>Th/<sup>238</sup>U) and (<sup>226</sup>Ra/<sup>230</sup>Th), excepting (<sup>230</sup>Th/<sup>238</sup>U) for BCR-1 that deviates by 4‰ outside of error and (<sup>226</sup>Ra/<sup>230</sup>Th) for TML-3 that deviates by 2‰ from equilibrium (brackets indicate activity ratios). On the basis of these results, we adopt 2 $\sigma$  precisions of 8‰ for (<sup>234</sup>U/<sup>238</sup>U), 2‰ for (<sup>238</sup>U/<sup>232</sup>Th), 1‰ for (<sup>230</sup>Th/<sup>232</sup>Th), 2‰ for (<sup>230</sup>Th/<sup>238</sup>U) and 6‰ for (<sup>226</sup>Ra/<sup>230</sup>Th) for the data.

**Table 1.** U Series Results for Secular Equilibrium Rock Standards and Interlaboratory Samples Over the Period 2007–2009

Standard/Rock	Th (ng/g)	U (ng/g)	$(^{234}\text{U}/^{238}\text{U})$	$(^{238}\text{U}/^{232}\text{Th})$	$(^{230}\text{Th}/^{232}\text{Th})$	$(^{230}\text{Th}/^{238}\text{U})$	$^{226}\text{Ra}$ (fg/g)	$(^{226}\text{Ra}/^{230}\text{Th})$
BCR-1	5.799	1.683	1.000	0.880	0.883	1.002	570.5	1.00
BCR-1	5.789	1.698	1.001	0.890	0.879	0.988	-	-
BCR-1	5.552	1.644	1.000	0.898	0.874	0.972	555.5	1.02
BCR-1 <sup>a</sup>	5.552	1.623	1.002	0.887	0.874	0.985	555.5	1.02
BCR-1 <sup>a</sup>	5.552	1.641	0.999	0.897	0.874	0.974	556.1	1.02
Average	5.649	1.658	1.000	0.891	0.876	0.984	559.4	1.02
2 std. dev.	0.266	0.063	0.002	0.015	0.008	0.024	14.8	0.03
BCR-2	5.649	1.665	1.000	0.894	0.879	0.983	-	-
BCR-2 <sup>a</sup>	5.739	1.665	1.000	0.880	0.877	0.996	549.1	0.97
BCR-2 <sup>a</sup>	5.754	1.665	1.000	0.878	0.875	0.996	543.1	0.97
Average	5.714	1.665	1.000	0.884	0.877	0.992	546.1	0.97
2 std. dev.	0.114	n/a	0.000	0.018	0.005	0.015	8.5	0.00
TML-3	29.182	10.186	1.010	1.059	1.089	1.028	3530.1	1.00
TML-3	27.504	9.826	1.003	1.084	1.083	0.999	3518.2	1.06
TML-3	29.627	10.582	1.006	1.084	1.077	0.993	-	-
TML-3	29.793	10.476	0.995	1.067	1.075	1.008	3550.0	1.00
TML-3	29.062	10.505	0.993	1.097	1.086	0.990	-	-
Average	29.034	10.315	1.002	1.078	1.082	1.004	3532.8	1.02
2 std. dev.	1.814	0.624	0.015	0.030	0.012	0.030	32.1	0.07
<i>2392-9 BBQ Flow</i>								
This study	0.117	0.047	0.996	1.217	1.346	1.106	48.9	2.78
Rubin <i>et al.</i> [2005]	0.117	0.048	-	1.246	1.392	1.117	-	2.64
Sims <i>et al.</i> [2002]	0.118	0.048	1.002	1.231	1.393	1.131	48.5	2.66

<sup>a</sup>Repeat measurements of U or Th only.

[12] Table 1 includes results from a MORB glass from the BBQ flow (sample 2392-9) from the East Pacific Rise [Haymon *et al.*, 1993; Rubin *et al.*, 1994]. The U, Th and  $^{226}\text{Ra}$  concentrations from the BBQ flow are in good agreement with Rubin *et al.* [2005] and Sims *et al.* [2002] although we obtained a  $(^{230}\text{Th}/^{238}\text{U})$  ratio that is closer to (and within our analytical reproducibility of) that reported by Rubin *et al.* [2005] than by Sims *et al.* [2002]. (Note that there is a typo in the work by Rubin *et al.* [2005], and sample 2392-1 is in fact 2392-9 (K. Rubin, personal communication, 2010).)

[13] The lower  $^{230}\text{Th}$  is the opposite to the effect of seawater alteration or manganese coatings. Because this sample has a very low Th concentration compared with most of the other samples and standards analyzed, it may reflect overcorrection for the  $^{232}\text{Th}$  tail on  $^{230}\text{Th}$  because of the linear extrapolation employed and we also obtained a higher  $(^{226}\text{Ra}/^{230}\text{Th})$  ratio for this sample. However, our  $(^{230}\text{Th}/^{238}\text{U})$  and  $(^{226}\text{Ra}/^{230}\text{Th})$  ratios are not reproducibly lower and higher, respectively, in the other standards analyzed and there may be real (minor) heterogeneity within the BBQ flow. Either way, the consequence of overcorrecting the  $^{230}\text{Th}$  tail would be that the U-Th disequilibria reported here would represent minimum values; higher  $(^{230}\text{Th}/^{232}\text{Th})$  ratios would only lead to an increase

in the number of samples inferred to have formed off axis (see below).

## 4. Results

[14] The reader is referred to Regelous *et al.* [1999] and Niu *et al.* [1999] for a detailed description and discussion of the major and trace element and Sr-Nd-Pb isotope characteristics and variations in the  $10^{\circ}30'\text{N}$  and  $11^{\circ}20'\text{N}$  traverse samples, respectively. Previously unpublished major and trace element data for the  $9^{\circ}30'\text{N}$  samples are provided in Table 2; U-Th and Pb isotope data for these samples can be found in work by Zou *et al.* [2002]. As illustrated in Figure 2, the vast majority of the samples are N-MORB basalts; seven are E-MORB. Although we largely restrict the discussion below to the basalts, a few of the samples are more evolved; four are basaltic andesites (PH103-2, PH46-3, PH79-2 and PH78-2) and one plots in the andesite field (PH79-1). However, it is unlikely that any of the samples have undergone fractional crystallization of accessory phases, such as apatite, that have the potential to affect U series disequilibria.

[15] The new U-Th-Ra results are presented in Table 3 and because the age of the samples is unknown, no age correction has been applied to any of the data. Seawater has high concentrations



**Table 2.** Major and Trace Element Data for 9°30'N Samples<sup>a</sup>

	P2-3	PH3-1	PH4-1	PH6-2	PH8-1	P10-2R	PH14-1	PH18-2	PH23-1	PH31-9	PH33-3	PH34-1	PH35-1	PH36-7	PH37-1
Latitude (N)	9.52	9.52	9.52	9.52	9.53	9.32	9.53	9.52	9.51	9.50	9.49	9.49	9.49	9.49	9.48
Longitude (W)	104.19	104.18	104.17	104.14	104.12	104.05	104.03	103.94	104.30	104.40	104.41	104.44	104.46	104.48	104.50
Water depth (m)	2888	2771	3018	2980?	2963	3123	2880	3080	2627	2891	2929	2800	2971	2787	2857
Dist. to ridge (km)	5.70	6.65	7.42	10.60	13.35	17.70	23.52	32.39	-6.88	-17.65	-20.96	-21.97	-24.73	-26.74	-28.38
Age (kyr)	104	121	135	193	243	322	428	589	125	321	381	399	450	486	516
SiO <sub>2</sub> (wt. %)	50.58	50.58	50.49	50.73	50.86		50.62	50.57	50.89	51.02	51.26	50.00	51.33	51.32	50.26
TiO <sub>2</sub>	1.61	1.61	1.61	1.71	1.73		1.30	2.14	1.54	1.92	1.77	1.89	2.45	1.56	1.75
Al <sub>2</sub> O <sub>3</sub>	14.55	14.55	15.12	14.36	14.33		14.99	14.10	14.75	14.23	14.22	15.94	13.22	14.49	15.63
FeO <sup>T</sup>	10.67	10.67	10.37	10.85	10.95		9.18	11.63	10.09	11.14	10.80	9.97	13.20	10.18	9.63
MnO	0.19	0.19	0.18	0.18	0.20		0.17	0.20	0.20	0.21	0.19	0.19	0.25	0.19	0.20
MgO	7.28	7.28	7.42	7.07	6.95		7.71	6.24	7.10	6.60	6.80	6.93	5.45	7.05	7.38
CaO	11.90	11.90	11.49	11.66	11.55		12.63	11.03	12.06	11.39	11.46	10.84	10.04	11.93	11.22
Na <sub>2</sub> O	2.58	2.58	2.64	2.72	2.77		2.75	3.07	2.66	2.81	2.78	3.11	3.20	2.67	2.88
K <sub>2</sub> O	0.10	0.10	0.12	0.13	0.11		0.09	0.22	0.10	0.13	0.12	0.42	0.19	0.10	0.38
P <sub>2</sub> O <sub>5</sub>	0.14	0.14	0.15	0.16	0.15		0.10	0.22	0.13	0.17	0.17	0.27	0.21	0.12	0.21
Total	99.60	99.60	99.58	99.58	99.59		99.54	99.41	99.53	99.62	99.56	99.55	99.54	99.62	99.54
Li (ppm)	5.6	5.6	5.5	5.6	6.6		4.3	6.6	5.2	6.8	5.6	5.9	7.6	4.9	5.0
Sc	42	42	38	45	47		43	45	52	46	45	38	44	44	43
V	272	272	270	288	309		239	324	353	336	305	267	362	292	300
Cr	288	288	274	182	193		381	163	345	187	210	246	45	197	277
Co	44	44	48	45	46		47	46	64	51	50	48	49	50	54
Ni	94	94	112	71	70		102	66	112	71	72	114	46	81	137
Cu	73	73	75	72	76		86	75	107	80	86	77	76	82	85
Zn	81	81	81	86	91		70	103	99	93	88	91	114	91	94
Ga	16	16	16	16	17		15	18	16	19	18	20	20	16	17
Rb	6.22	0.64	0.94	0.93	0.75	5.53	0.47	2.31	0.83	0.95	0.84	6.43	1.53	0.68	6.10
Sr	199	102	118	110	113	205	118	139	112	117	117	230	122	104	193
Y	37	30	30	30	32	30	20	37	27	34	29	29	41	26	26
Zr	161	91	97	89	98	123	65	133	83	108	92	124	137	76	111
Nb	11.93	2.03	2.85	2.53	2.37	10.38	1.44	5.03	2.22	2.67	2.49	11.13	3.84	1.91	9.76
Cs		0.01	0.01	0.01	0.01		0.01	0.04	0.01	0.01	0.01	0.08	0.03	0.01	0.10
Ba	77.4	5.8	9.1	9.3	7.7	93.3	5.1	25.1	10.8	9.5	9.5	96.6	15.2	7.4	79.1
La	9.88	2.82	3.56	3.42	3.54	8.59	2.39	6.02	3.27	4.26	3.76	9.82	5.82	2.97	8.77
Ce	25.41	9.38	11.23	10.80	11.60	21.74	7.83	17.74	10.38	13.79	11.89	24.16	17.85	9.47	21.29
Pr	4.03	1.75	2.02	1.97	2.16	3.41	1.46	3.12	1.91	2.54	2.17	3.69	3.25	1.78	3.25
Nd	18.02	9.04	10.06	9.82	10.88	15.32	7.37	14.96	9.68	12.73	10.91	16.21	15.94	9.02	14.02
Sm	5.40	3.17	3.33	3.38	3.73	4.36	2.50	4.83	3.31	4.34	3.65	4.58	5.32	3.09	3.97
Eu	1.85	1.17	1.21	1.24	1.36	1.53	0.99	1.65	1.22	1.58	1.33	1.60	1.82	1.18	1.38
Gd	7.04	4.87	4.94	5.13	5.54	5.63	3.70	6.78	4.83	6.22	5.35	5.57	7.50	4.76	5.04
Tb	1.06	0.79	0.78	0.82	0.89	0.86	0.60	1.06	0.77	0.99	0.86	0.86	1.19	0.78	0.79
Dy	7.12	5.47	5.54	5.68	6.20	5.80	4.04	7.38	5.34	6.83	5.94	5.78	8.25	5.43	5.48

Table 2. (continued)

	P2-3	PH3-1	PH4-1	PH6-2	PH8-1	P10-2R	PH14-1	PH18-2	PH23-1	PH31-9	PH33-3	PH34-1	PH35-1	PH36-7	PH37-1
Ho	1.48	1.18	1.16	1.21	1.31	1.21	0.86	1.55	1.13	1.45	1.25	1.18	1.78	1.16	1.14
Er	4.38	3.46	3.49	3.61	3.91	3.58	2.53	4.62	3.46	4.36	3.76	3.51	5.29	3.48	3.44
Tm	0.61	0.48	0.48	0.50	0.53	0.49	0.34	0.62	0.46	0.59	0.50	0.47	0.72	0.49	0.46
Yb	3.97	3.25	3.25	3.35	3.60	3.27	2.36	4.24	3.14	3.96	3.39	3.19	4.82	3.19	3.08
Lu	0.61	0.49	0.49	0.50	0.54	0.49	0.34	0.64	0.47	0.60	0.52	0.48	0.74	0.49	0.47
Hf	4.45	2.74	2.83	2.75	3.06	3.67	2.07	4.17	2.72	3.43	2.98	3.64	4.44	2.66	3.41
Ta	0.95	0.16	0.22	0.19	0.18	0.71	0.13	0.38	0.17	0.23	0.21	0.76	0.31	0.26	0.71
Pb	0.90	0.39	0.45	0.43	0.47	0.87	0.50	0.65	0.45	0.51	0.44	0.83	0.70	0.41	0.78
Th	0.751	0.106	0.162	0.157	0.149	0.450	0.098	0.363	0.162	0.213	0.190	0.978	0.326	0.144	0.965
U	0.259	0.046	0.066	0.062	0.063	0.149	0.044	0.143	0.063	0.089	0.078	0.327	0.135	0.062	0.305

<sup>a</sup>Analyses were performed on picked and leached glass chips following methods described by Niu *et al.* [1999] and Regelous *et al.* [1999].

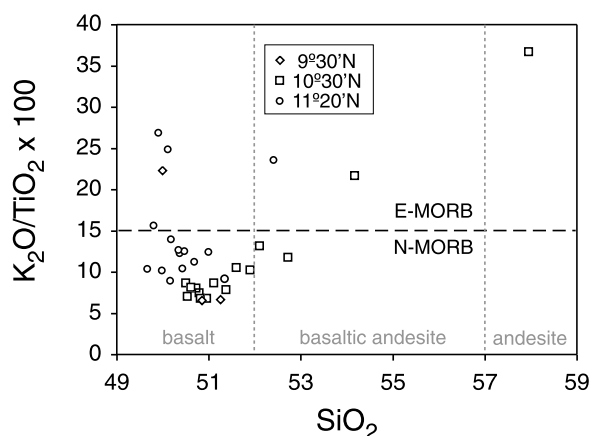


Figure 2. Plot of  $K_2O/TiO_2 \times 100$  versus  $SiO_2$  showing that the majority of the samples are N-MORB basalts.

of  $^{234}U$ ,  $^{230}Th$  and  $^{226}Ra$  that could be inherited in Mn coatings on MORB glasses [Chen *et al.*, 1986]. The leachates have ( $^{234}U/^{238}U$ ) ratios that range from 1.028 to 1.103 and unrealistically high ( $^{230}Th/^{232}Th$ ) and ( $^{230}Th/^{238}U$ ) ratios (see Table 3). However, with the exception of 3 of the samples, the ( $^{234}U/^{238}U$ ) ratios of the leached glasses all lie within  $2\sigma$  analytical error of secular equilibrium (Figure 3) and omitting the 3 outliers (PH10-2, PH63-1 and PH54-3) does not alter any of the conclusions reached below. Thus, the sample preparation procedures appear to have effectively removed the effects of Mn coatings and/or seawater alteration. Note that Figure 3 also shows that there is no correlation between ( $^{234}U/^{238}U$ ) and ( $^{230}Th/^{238}U$ ). Duplicate samples from the same dredges (i.e., PH8-1 and PH8-3, PH79-1 and PH79-2) and a duplicate analysis of the same sample (PH33-3) yielded ( $^{230}Th/^{238}U$ ) ratios that were reproducible within the precision estimates adopted above (Table 3). For clarity we begin by discussing the U-Th-Ra results from each traverse separately.

#### 4.1. Samples at 9°30'N

[16] We obtained contrasting results to those of Zou *et al.* [2002] for the four most anomalous samples in their study. Our U and Th concentrations are in good agreement with the exception of sample PH34-1 that has a higher concentration of Th than those reported by Zou *et al.* [2002]. Compared to the Zou *et al.* [2002] data, sample PH33-3 has lower U/Th and ( $^{230}Th/^{232}Th$ ) ratios and a 1.5% measured  $^{230}Th$  excess. This is within error of secular equilibrium but this sample also has 25%  $^{226}Ra$  excess suggesting that sample represents an



**Table 3.** U Series Measurements of EPR Samples, Ordered From West to East Across Each Traverse

Sample Number	Longitude (W)	Latitude (N)	Depth (m)	Distance to Ridge (km)	Spreading Age (kyr)	Th (ng/g)	U (ng/g)	$(^{234}\text{U}/^{238}\text{U})$	$(^{238}\text{U}/^{232}\text{Th})$	$(^{230}\text{Th}/^{232}\text{Th})$	$(^{230}\text{Th}/^{238}\text{U})$	$^{226}\text{Ra}$ (fg/g)	$(^{226}\text{Ra}/^{230}\text{Th})$
<i>9°30'N</i>													
PH33-3	104.4067	9.4932	2929	-20.96	381	0.143	0.060	0.995	1.274	1.284	1.015	25.77	1.25
Duplicate						0.160	0.065	1.007	1.222	1.258	1.029	-	-
PH34-1	104.2627	9.2929	2800	-22.00	400	0.733	0.253	0.994	1.047	1.031	0.991	88.14	1.04
PH8-1	104.0775	9.3150	2963	13.30	242	0.138	0.059	0.999	1.288	1.284	1.000	-	-
PH8-3	104.0775	9.3150	2963	13.30	242	0.137	0.058	1.003	1.285	1.264	0.985	20.59	1.07
PH10-2	104.0471	9.3187	3123	17.70	322	0.450	0.149	1.009	1.005	1.045	1.039	-	-
<i>10°30'N</i>													
PH79-1	103.8792	10.4237	3097	-30.39	552	1.554	0.572	0.996	1.116	1.139	1.020	-	-
PH79-2	103.8792	10.4237	3097	-30.39	552	1.144	0.434	0.993	1.150	1.162	1.011	-	-
PH78-2	103.8628	10.4267	3058	-28.48	518	0.659	0.258	0.999	1.189	1.205	1.013	91.08	1.03
PH70-2	103.6983	10.4718	3007	-9.02	164	0.218	0.081	1.008	1.124	1.175	1.046	32.95	1.58
PH65-1	103.6368	10.4543	2996	-3.56	65	0.276	0.106	0.993	1.164	1.260	1.082	41.36	1.06
PH63-1	103.6188	10.4763	2832	0.45	8	0.303	0.112	1.009	1.123	1.308	1.165	97.77	2.20
PH62-1	103.6127	10.4802	2812	0.84	15	0.267	0.102	1.004	1.160	1.344	1.159	73.49	1.83
PH64-3	103.6252	10.4548	3008	2.99	54	0.277	0.105	1.005	1.156	1.303	1.128	39.19	0.97
PH55-3	103.5317	10.4865	3170	10.14	184	0.274	0.097	1.005	1.074	1.116	1.039	33.76	0.99
PH54-3	103.5133	10.4983	3069	12.39	225	0.157	0.059	1.010	1.142	1.187	1.039	-	-
PH52-2	103.4865	10.5022	3053	15.50	282	0.262	0.102	1.003	1.183	1.285	1.087	55.70	1.48
PH49-2	103.4210	10.5165	3214	23.20	422	0.553	0.219	0.992	1.199	1.249	1.042	74.83	0.97
PH47-3	103.3812	10.5178	3192	27.69	503	0.529	0.201	0.999	1.150	1.180	1.026	-	-
PH46-3	103.3743	10.5195	3066	28.49	518	1.002	0.392	0.994	1.185	1.194	1.008	-	-
PH45-1	103.3590	10.5358	3169	30.57	556	0.665	0.260	0.994	1.184	1.204	1.017	-	-
<i>11°20'N</i>													
PH108-1	103.7940	11.3423	2724	-2.73	50	0.788	0.283	0.997	1.088	1.289	1.185	-	-
Leachate						2.647	0.245	1.028	0.281	1.690	6.015	-	-
PH104-1	103.7770	11.3443	2364	-1.95	35	0.282	0.110	0.995	1.188	1.351	1.137	83.69	1.96
Leachate						0.680	0.408	1.095	1.820	3.604	1.980	-	-
PH102-1	103.7778	11.3575	2625	0.40	7	0.277	0.100	1.002	1.103	1.296	1.175	79.76	1.99
PH103-2	103.7803	11.3677	2570	0.94	17	0.983	0.372	0.995	1.149	1.306	1.137	-	-
Leachate						0.288	0.311	1.103	3.273	5.098	1.558	-	-
PH101-1	103.7708	11.3565	2505	1.18	21	0.305	0.116	1.004	1.156	1.330	1.150	54.39	1.20
PH100-1	103.7633	11.3572	2623	2.03	37	0.272	0.106	1.006	1.187	1.376	1.160	32.08	0.93
PH99-2	103.7602	11.3585	2830	2.38	43	0.240	0.095	1.008	1.202	1.383	1.150	-	-
PH94-1	103.7090	11.3692	2863	8.58	156	0.324	0.114	1.004	1.067	1.127	1.055	-	-
PH92-1	103.6775	11.3817	2900	12.57	228	0.681	0.240	1.008	1.069	1.127	1.054	98.23	1.14
PH91-1	103.6560	11.3802	3101	15.06	274	0.131	0.054	0.995	1.241	1.252	1.017	22.30	1.21
PH89-1	103.6118	11.3890	2979	20.46	372	0.386	0.145	0.993	1.143	1.120	0.980	51.14	1.06
PH88-1	103.5968	11.3843	3008	22.15	403	0.217	0.087	0.997	1.214	1.193	0.987	31.52	1.09
PH84-1	103.5292	11.4123	3051	30.73	559	0.314	0.120	1.003	1.154	1.161	1.006	-	-
PH83-1	103.4298	11.4232	2996	42.66	776	0.341	0.124	1.008	1.105	1.131	1.024	40.95	0.95
PH82-1	103.3850	11.4272	2946	48.04	873	0.247	0.101	0.998	1.245	1.227	0.990	35.44	1.04

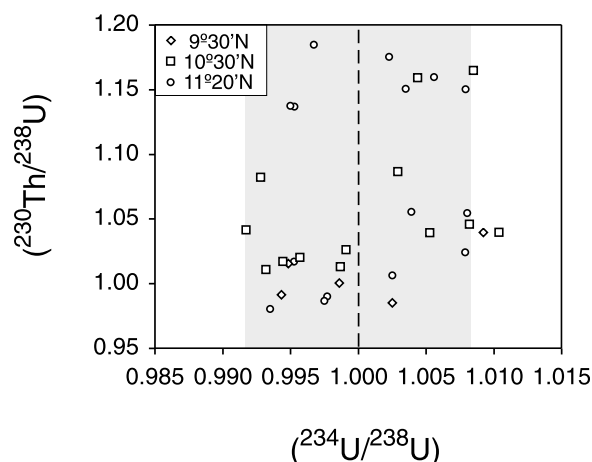


**Figure 3.** Plot of  $(^{230}\text{Th}/^{238}\text{U})$  versus  $(^{234}\text{U}/^{238}\text{U})$  showing that the vast majority of the samples have  $(^{234}\text{U}/^{238}\text{U})$  within  $2\sigma$  analytical error (8‰) of secular equilibrium (gray field) and that there is no correlation with the extent of U-Th disequilibria. Dashed line indicates secular equilibrium.

off-axis eruption (see below). Sample PH8-1 is in U-Th isotopic equilibrium whereas sample PH8-3, from the same dredge, is also essentially indistinguishable from secular equilibrium. We suggest that both of these latter two samples are effectively in secular equilibrium (and thus could have formed at the ridge axis). This is in contrast to the 13%  $^{230}\text{Th}$  excess reported by Zou *et al.* [2002] for PH8-1. The biggest difference between the two studies is that samples PH34-1 and PH10-2, that had significant  $^{238}\text{U}$  excesses in the previous work, are either within error of secular equilibrium (sample PH34-1) or have a small but significant (4%)  $^{230}\text{Th}$  excess (sample PH10-2). On the U-Th equiline diagram, three of the samples lie close to the equiline at high U/Th whereas the remaining two lie at low U/Th, one with  $^{230}\text{Th}$  excess (Figure 4a).

#### 4.2. Samples at 10°30'N

[17] The samples from this traverse have Th and U concentrations that range from 0.16 to 1.55 and 0.06 to 0.57 ppm, respectively, which are in good agreement with ICP-MS concentration data presented by Regelous *et al.* [1999].  $^{226}\text{Ra}$  concentrations range from 33 to 98 fg/g overlapping the range observed by Lundstrom *et al.* [1999] and Sims *et al.* [2002, 2003].  $(^{230}\text{Th}/^{232}\text{Th})$  ranges from 1.12 to 1.34 and the majority of the samples have  $^{230}\text{Th}$  excess with  $(^{230}\text{Th}/^{238}\text{U})$  ranging from within error of secular equilibrium up to 17%. Of the samples successfully analyzed for  $^{226}\text{Ra}$  (some TIMS analysis runs failed), four are within analytical error of

secular equilibrium while the remaining four have significant  $^{226}\text{Ra}$  excesses (PH52-2, PH70-2, PH62-1 and PH63-1) with  $(^{226}\text{Ra}/^{230}\text{Th})$  ratios that varies from 1.5 to 2.2.

[18] On the U-Th equiline diagram, three of the 10°30'N samples lie parallel to, and overlap, the

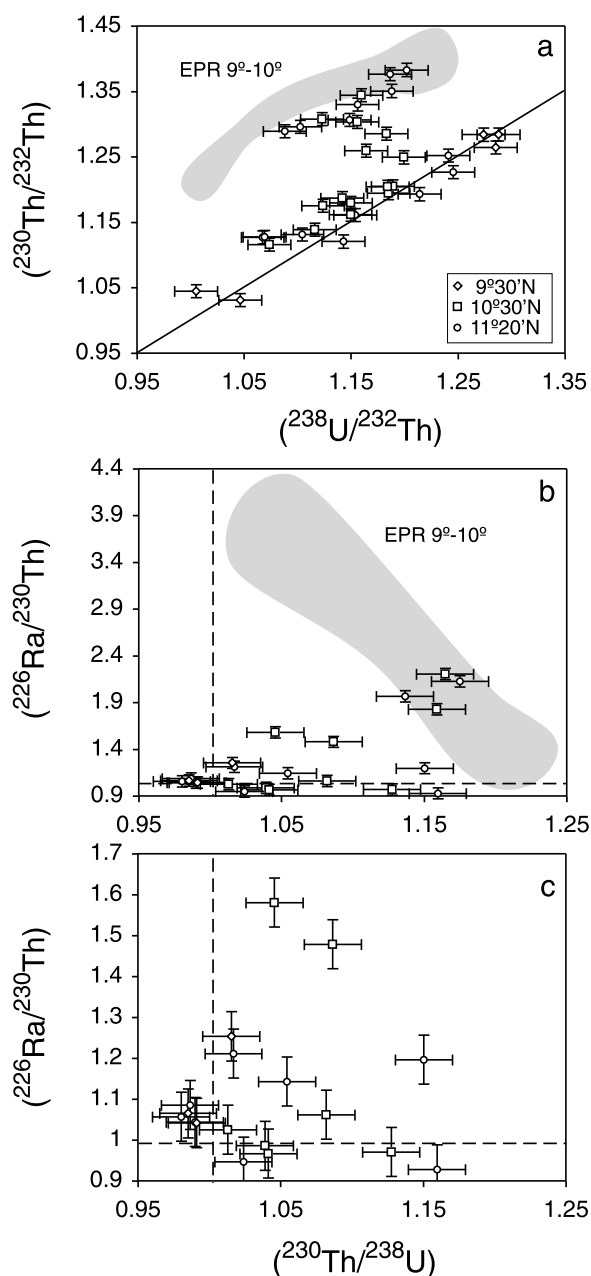


**Figure 4.** (a) U-Th equiline diagram, (b)  $(^{226}\text{Ra}/^{230}\text{Th})$  versus  $(^{230}\text{Th}/^{238}\text{U})$  diagram, and (c) an expansion of the lower part of the  $(^{226}\text{Ra}/^{230}\text{Th})$  versus  $(^{230}\text{Th}/^{238}\text{U})$  diagram (error bars are  $2\sigma$ ). Also shown is the field for axial MORB samples from the region 9°–10°N on the EPR (data from Lundstrom *et al.* [1999] and Sims *et al.* [2002]). Dashed lines indicate secular equilibrium.

field for 9°30'–50'N axial samples [Lundstrom *et al.*, 1999; Sims *et al.*, 2002], nine lie close to the equiline and three plot in between these two groups (Figure 4a). Note that this field encompasses N-, E- and D-MORBs each with their own source chemistry and conditions of petrogenesis. On a plot of ( $^{226}\text{Ra}/^{230}\text{Th}$ ) versus ( $^{230}\text{Th}/^{238}\text{U}$ ), two samples lie within the negatively sloped EPR array of Sims *et al.* [2002]. The remainder fall below this array and/or within error of secular equilibrium. This is consistent with decay since the true age of the samples is unknown (see below).

### 4.3. Samples at 11°20'N

[19] Samples from the 11°20'N traverse show slightly more restricted Th and U concentrations that range from 0.13 to 0.98 and 0.05 to 0.37 ppm, respectively, but again agree well with ICP-MS concentration data from Niu *et al.* [1999].  $^{226}\text{Ra}$  concentrations range from 22 to 98 fg/g, again overlapping that observed in data from Sims *et al.* [2002, 2003]. ( $^{230}\text{Th}/^{232}\text{Th}$ ) ranges from 1.12 to 1.38 and two samples have ( $^{230}\text{Th}/^{238}\text{U}$ ) less than, but within error of, 1. The majority of the remaining samples have  $^{230}\text{Th}$  excess with ( $^{230}\text{Th}/^{238}\text{U}$ ) ratios ranging up to 1.19. Samples PH82-1, PH89-1, PH100-1 and PH83-1 all have ( $^{226}\text{Ra}/^{230}\text{Th}$ ) ratios that are effectively in secular equilibrium. In the remaining six samples ( $^{226}\text{Ra}/^{230}\text{Th}$ ) ratios range from 1.09 to 2.13 (PH88-1, PH92-1, PH91-1, PH101-1, PH104-1 and PH102-1).

[20] On the U-Th equiline diagram, the 11°20'N samples form a bimodal distribution and overlap the two main groups from 10°30'N samples. Within these two arrays ( $^{230}\text{Th}/^{232}\text{Th}$ ) is strongly correlated with ( $^{238}\text{U}/^{232}\text{Th}$ ), commonly ascribed to source composition [e.g., Goldstein *et al.*, 1992]. Seven samples fall within or close to the EPR 9°30'–50'N axial array whereas the remainder scatter around the equiline (Figure 4a). On the ( $^{226}\text{Ra}/^{230}\text{Th}$ ) versus ( $^{230}\text{Th}/^{238}\text{U}$ ) plot, the 11°20'N samples again overlap the 10°30'N samples and two samples lie within the Sims *et al.* [2002] EPR array, indicating that their ( $^{226}\text{Ra}/^{230}\text{Th}$ ) ratios may be near primary. Again, the remainder fall below this and/or within error of secular equilibrium (Figures 4b and 4c) suggestive of decay since eruption.

## 5. Off-Axis Eruptions

[21] In Figures 5 and 6, we plot the U series disequilibria against distance from the ridge axis for all three traverses (error bars are  $2\sigma$ ). The half-life

of  $^{230}\text{Th}$  is 75 kyr and so the resolution of the  $^{230}\text{Th}$ - $^{238}\text{U}$  system is, in principle, ~600 kyr, corresponding to a distance of ~33 km for the EPR half-spreading rate. The U-Th data are compared with two decay curves that assume a half-spreading rate of 5.5 cm/yr and initial, ridge-formed ( $^{230}\text{Th}/^{238}\text{U}$ ) ratios of 1.19 and 1.11 that correspond to the highest and lowest values, respectively, reported by Sims *et al.* [2002] for 9°30'–50'N axial EPR samples. While these data are clearly pertinent to the 9°30'N traverse, they might be considered less so for the other two traverses further north. However, U-Th data extending as far north as 10°N are consistent with the maximum axial ( $^{230}\text{Th}/^{238}\text{U}$ ) ratios being ~1.17–1.19 [Lundstrom *et al.*, 1999]. Moreover, the initial ( $^{230}\text{Th}/^{238}\text{U}$ ) would have to be >2 in order for all of the samples to lie on or below the axial decay curves and this value significantly exceeds any MORB measurement worldwide [Elliott and Spiegelman, 2003].

[22] Zou *et al.* [2002] did not undertake  $^{226}\text{Ra}$  measurements in their study, but Figures 5d–5f show plots of Ra-Th disequilibria against distance from the ridge axis for all three traverses along with a decay curve based on the highest ( $^{226}\text{Ra}/^{230}\text{Th}$ ) ratio (4.2) measured by Lundstrom *et al.* [1999]. Note that the short (1.6 kyr) half-life of  $^{226}\text{Ra}$  means that any sample formed at the ridge axis will have returned to  $^{226}\text{Ra}$ - $^{230}\text{Th}$  equilibrium within 10 kyr, or a distance of only 0.5 km for the EPR spreading rate. Alteration might lead to  $^{226}\text{Ra}$  excesses but the samples have ( $^{234}\text{U}/^{238}\text{U}$ ) within error of secular equilibrium and excessive leaching would be unlikely to produce ( $^{226}\text{Ra}/^{230}\text{Th}$ ) > 1. It has also been suggested that diffusive interaction between melt and cumulate plagioclase could lead to  $^{226}\text{Ra}$  excesses in MORB [Saal and Van Orman, 2004]. However, that would not significantly alter the time scale implications made below. Note also that, because the age of the samples is unknown, the measured ( $^{226}\text{Ra}/^{230}\text{Th}$ ) ratios should be regarded as minima. Samples with  $^{226}\text{Ra}$  excess beyond analytical uncertainty are identified in Figures 5a–5c by gray filled symbols.

[23] Finally, Sims *et al.* [2003] have demonstrated that eruptions can occur up to 4 km off axis at 9°50'N on the EPR consistent with the suggestion of Perfit and Chadwick [1998]. Indeed, the last eruption in this area flowed 2+ km away from the ridge axis and erupted in places from vents that were almost a km off axis [Soule *et al.*, 2007]. Thus, we also show a set of dashed gray curves in Figure 5 which permit that the samples were emplaced up to 4 km off axis with an initial ( $^{230}\text{Th}/^{238}\text{U}$ ) ratio of 1.19 and an initial ( $^{226}\text{Ra}/^{230}\text{Th}$ ) ratio of 4.2. This probably

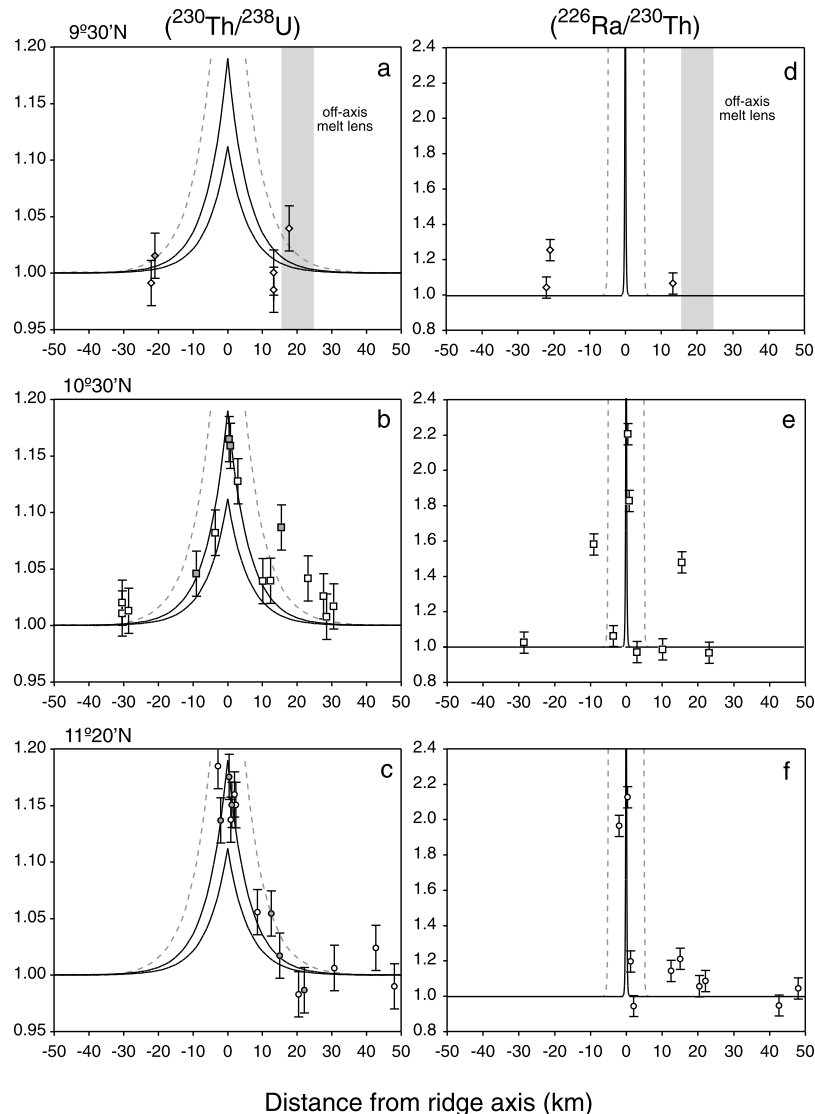


**Figure 5.** Plots of ( $^{230}\text{Th}/^{238}\text{U}$ ) and ( $^{226}\text{Ra}/^{230}\text{Th}$ ) versus distance either side of the ridge axis for the three traverses (error bars are  $2\sigma$ ). Solid curves show decay of axially formed disequilibria, assuming a half-spreading rate of 5.5 cm/yr. For ( $^{230}\text{Th}/^{238}\text{U}$ ), these assumed maximum and minimum initial ratios of 1.19 and 1.11 as measured in axially formed samples from 9°30'–50°N [Sims *et al.*, 2002]. The decay curve for ( $^{226}\text{Ra}/^{230}\text{Th}$ ) assumed an initial ratio of 4.2 as measured on the A-B transform [Lundstrom *et al.*, 1999]. The dashed curves reflect the same model but allow for the lavas to have formed at the edge of the neovolcanic zone that is thought to be up to 8–10 km wide [e.g., Perfit *et al.*, 1994; Sims *et al.*, 2003]. Samples lying above the decay curves are inferred to have formed off axis, and those samples with significant  $^{226}\text{Ra}$  excess are indicated by gray symbols on the ( $^{230}\text{Th}/^{238}\text{U}$ ) diagrams. The shaded bar on the 9°30'N traverse indicates the location of the melt lens identified seismically by Durant and Toomey [2009].

represents an extreme case, since most of the off-axis samples analyzed by Sims *et al.* [2003] had somewhat lower ( $^{230}\text{Th}/^{238}\text{U}$ ) and ( $^{226}\text{Ra}/^{230}\text{Th}$ ) ratios than their axial samples. Nevertheless, these curves allow us to distinguish any samples that erupted >4 km from the axis.

[24] In the case of samples for which the data overlap, within error, or lie beneath the decay

curves there is no reason, from a U series isotope perspective, to suspect that they did not erupt at the ridge axis and become subsequently transported outward with the plate. On this basis, only one of the four 9°30'N samples (PH10-2) lie above the U-Th decay curves but that sample could, within error, have formed 4 km off axis (gray dashed curve in Figure 5a). Problematically, this is one of

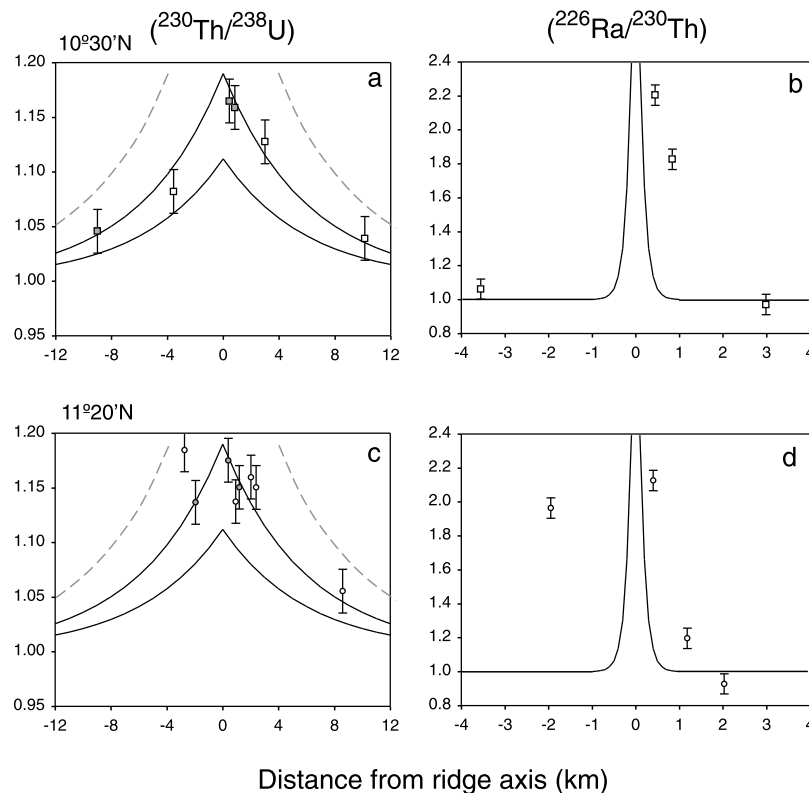


**Figure 6.** Expanded view of the near-axis region for the 10°30'N and 11°20'N traverses.

the samples with a measured  $(^{234}\text{U}/^{238}\text{U})$  outside of analytical error from equilibrium. However, one sample ~20 km to the west of the ridge (PH33-3) which lies above, but overlaps within error, the U-Th decay curves also has significant  $^{226}\text{Ra}$  excess indicating that this sample formed off axis close to its present location. Note that the combination of large  $^{226}\text{Ra}$  excess with low  $(^{230}\text{Th}/^{238}\text{U})$  is consistent with the negative  $(^{226}\text{Ra}/^{230}\text{Th}) - (^{230}\text{Th}/^{238}\text{U})$  array found in EPR samples [Sims *et al.*, 2002].

[25] At 10°30'N, two samples 10–20 km to the east of the ridge clearly lie outside of error above all three of the U-Th decay curves while the remaining thirteen lie within error of them. One of these samples (PH52-2) has significant  $^{226}\text{Ra}$  excess, as does one sample ~10 km to the west of the ridge (PH70-2) that lies within error of the decay curves. Looking an expanded view close to the ridge axis (Figures 6a and 6b), all samples overlap the U-Th decay curves yet two lie above the  $^{226}\text{Ra}$  decay curve suggesting eruption a few km outside of the neovolcanic zone.

[26] Finally at 11°20'N, one sample to the far east of the ridge (PH83-1) lies just above the three U-Th

decay curves while the remaining fourteen lie within error of them. However, a further three of the eastern samples have significant  $^{226}\text{Ra}$  excess, again implying off-axis eruption. Close to the ridge axis, one sample (PH108-1) lies above the two axial U-Th decay curves but could still have formed within 4 km of the axis while a further three samples have  $^{226}\text{Ra}$  excesses suggesting that they must also have formed a few km outside of the neovolcanic zone (Figures 6c and 6d).

[27] In summary, our new data do not confirm the Zou *et al.* [2002] finding of large (i.e., axial magnitude)  $^{230}\text{Th}$  excesses 10–20 km either side of the ridge at 9°30'N. Furthermore, no significant  $^{238}\text{U}$  excesses have been found on any of the traverses [cf. Zou *et al.*, 2002]. Close to the axis, our data support suggestions [e.g., Perfit and Chadwick, 1998; Sims *et al.*, 2003; Soule *et al.*, 2005] that volcanism extends several km beyond the neovolcanic zone (Figure 6). If this is taken into account in our models (i.e., the dashed gray curves in Figures 5 and 6), then 80% of the samples formed in the neovolcanic zone and aged with the plate as it migrated outward. These data are con-



sistent with the observed alteration state of the samples.

[28] Nevertheless, our data also permit that seven of the samples formed more than 4 km from the axis. Three of these have small to moderate  $^{230}\text{Th}$  excesses and could have erupted within  $\sim 10$  km of their present location. However, 5 samples have  $^{226}\text{Ra}$  excesses suggesting that they erupted within  $\sim 0.5$  km of their present location. This reinforces the conclusion of *Zou et al.* [2002] that MORB eruptions are not restricted to within a few km either side of the ridge axis [e.g., *Goldstein et al.*, 1994; *Rubin et al.*, 1994; *Sims et al.*, 2003] but can occur as far out as 20 km through crust that is up to 550 kyr old (see Figure 5). The majority of the samples were dredged from small fault scarps [*Batiza et al.*, 1996] that could reflect the tensile fractures predicted by *Sohn and Sims* [2005] and some of these may have provided pathways for magma extrusion. It is also possible that some of the samples not analyzed for  $^{226}\text{Ra}$ , but lying on the axis U-Th decay curves, were also erupted off axis. These observations challenge the hypothesis that accretion of the crust is complete within a few km of the ridge axis and models that invoke highly efficient melt focusing [e.g., *Spiegelman and McKenzie*, 1987; *Korenaga and Kelemen*, 1997; *Fornari et al.*, 2004]. They also imply that not all of the samples from the traverses record the temporal evolution of MORB magmatism at the axis [cf. *Batiza et al.*, 1996; *Regelous et al.*, 1999; *Niu et al.*, 1999] (possibly explaining some of the scatter in the published trends) but may instead contain important information about melt generation beyond the axial zone [*Niu et al.*, 1996].

[29] Before we explore some of the further implications of the potential off-axis eruptions we recall that there is both seismic data [*Garmany*, 1989] and active seamounts on  $>1$  Myr crust [e.g., *Fornari et al.*, 1988; *Batiza et al.*, 1990; *Niu and Batiza*, 1997; *Niu et al.*, 1996] that provide compelling evidence for active magmatism up to 20–40 km from the ridge axis. In particular, *Durant and Toomey* [2009] found seismic evidence for a 5 km wide melt body 2 km deep beneath the Cocos plate 20 km to the east of the EPR axis at  $9^{\circ}30'\text{N}$  (see Figure 5a). Figure 5 suggests that off-axis volcanism occurs in roughly this location on the  $10^{\circ}30'\text{N}$  traverse as well. Importantly, our data also suggest off-axis eruption to the west, on the Pacific plate (see Figure 5), and this is consistent with the observations of significant U-Th disequilibria in samples from the Lamont seamounts [*Lundstrom et al.*, 1999]. However, with the present coverage there

appears to be no simple pattern to the distribution of the few inferred off-axis eruptions.

## 6. Origin of Low ( $^{230}\text{Th}/^{238}\text{U}$ ) Ratios in Off-Axis Samples

[30] One aspect of our data is that the subset of samples inferred to have erupted off axis may afford the possibility to interrogate melting dynamics beneath the EPR over a wider across-axis area that had previously been thought possible. In this respect, one of the most intriguing issues with the observations is that even those off-axis samples with significant  $^{226}\text{Ra}$  excess still have lower ( $^{230}\text{Th}/^{238}\text{U}$ ) than MORB erupted at the ridge axis (for these samples, the measured ( $^{230}\text{Th}/^{238}\text{U}$ ) can be considered primary). A similar observation is apparent in other data sets although its significance has not been discussed. Off-axis samples from the Southwest Indian Ridge have lower ( $^{230}\text{Th}/^{238}\text{U}$ ) and ( $^{226}\text{Ra}/^{230}\text{Th}$ ) than axial samples [*Standish and Sims*, 2010], and *Lundstrom et al.* [1999] found that ( $^{230}\text{Th}/^{238}\text{U}$ ) ratios decreased with distance from the EPR ridge axis across the Lamont seamounts. For example, *Lundstrom et al.* [1999] reported an analysis from the Siqueiros Transform with ( $^{230}\text{Th}/^{238}\text{U}$ ) of 1.01 in a sample that had ( $^{226}\text{Ra}/^{230}\text{Th}$ )  $> 3$ . Even EPR samples taken within 4 km of the ridge axis exhibit less U-Th-Ra disequilibria than those formed at the ridge axis [*Sims et al.*, 2003]. This suggests that the off-axis samples were derived from magmas that had lower initial ( $^{230}\text{Th}/^{238}\text{U}$ ) and we note in passing that this may compromise age determinations that assume a generic axial ( $^{230}\text{Th}/^{238}\text{U}$ ) value. Possible explanations for lower initial ( $^{230}\text{Th}/^{238}\text{U}$ ) ratios off axis include the role of source heterogeneity and changes in melting conditions.

### 6.1. The Role of Source Heterogeneity

[31] Numerous studies have argued that there is evidence for heterogeneities in the MORB source and some have argued that this could provide an important control on U series disequilibria [e.g., *Lundstrom et al.*, 1998; *Russo et al.*, 2009]. Indeed, *Davies* [2009] has recently argued for intimate mixing between melts from both depleted and enriched sources beneath all ridges and inferred that the enriched components are sourced from ancient recycled mafic material (e.g., pyroxenite [cf. *Sobolev et al.*, 2007]). *Perfit et al.* [1994] noted the intimate juxtaposition of N-MORB and E-MORB across the EPR, and some of our samples do have E-MORB

compositions (cf. Figure 2). Furthermore, the samples from 11°20'N show a significant range in radiogenic isotope composition demanding source heterogeneity [Niu *et al.*, 1999].

[32] Experiments have shown that pyroxenite has a higher melt productivity (%/GPa decompression) than peridotite [Petermann and Hirschmann, 2003]. U-Th disequilibria are highly sensitive to melting rate (see discussion below) and the faster melting rate of pyroxenite should result in lowered  $^{230}\text{Th}$  excesses [Prytulak and Elliott, 2009; Russo *et al.*, 2009], all else being equal. A caveat to this is that Elkins *et al.* [2008] have suggested that the higher partition coefficient for U relative to Th in pyroxenite would offset the effects of the faster melting rate. Nevertheless, in principle, the presence of pyroxenite in the melting region could explain the lower ( $^{230}\text{Th}/^{238}\text{U}$ ) ratios in off-axis samples, although this would require that pyroxenite is fortuitously present off axis but not beneath the neovolcanic zone [cf. Zou *et al.*, 2002]. How-

ever, we did not find any correlation between the U series disequilibria and radiogenic isotopes. Furthermore, the P/Nd ratios of the EPR traverse samples average  $62 \pm 9$ , apparently precluding a significant role for pyroxenite [O'Neill and Mallmann, 2007]. We conclude that there is no convincing evidence that the lowered  $^{230}\text{Th}$  excesses in the inferred off-axis samples reflect source heterogeneity [cf. Zou *et al.*, 2002]. Therefore, it is likely that any putative recycled components (as indicated by trace element or radiogenic isotope data) are present in the form of peridotite that has been metasomatized by pyroxenite melts rather than pyroxenite itself [e.g., Niu and O'Hara, 2008; Elkins *et al.*, 2008; Prytulak and Elliott, 2009].

## 6.2. Variations in Melting Conditions

[33] An alternative explanation for the decrease in primary ( $^{230}\text{Th}/^{238}\text{U}$ ) ratios away from the ridge axis is a change in the melt regime between axial and off-axis melt production. Models for the generation of U series disequilibria in MORB have

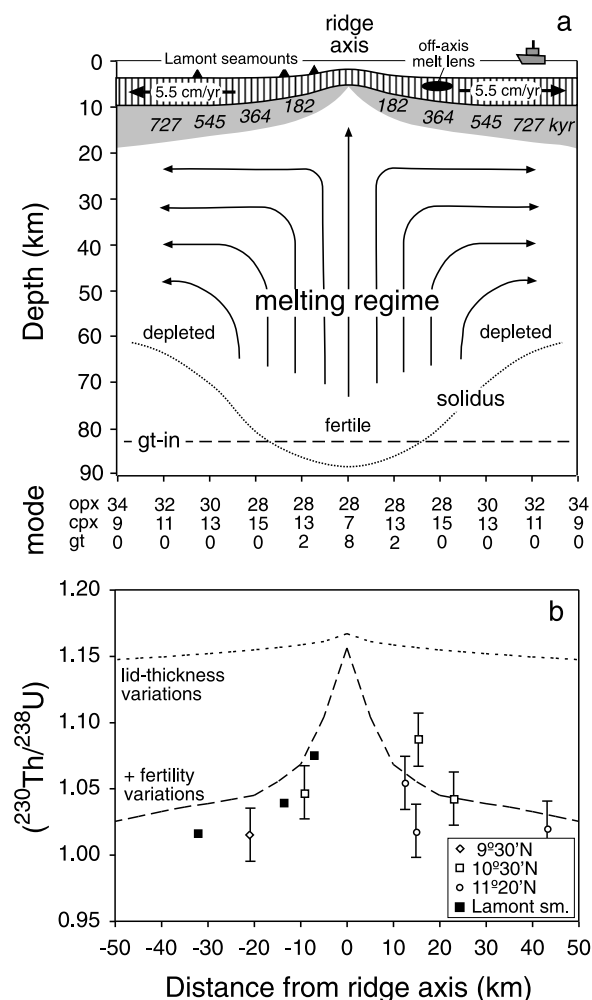


**Figure 7.** (a and b) Illustration of possible melting models to explain decreased, off-axis ( $^{230}\text{Th}/^{238}\text{U}$ ) ratios using the dynamic melting model of Williams and Gill [1989] and input parameters given in Table 4. In the first model, shown as the short-dashed curve in Figure 7b, the length of the melting column decreases away from the axis solely as a result of thickening of the overlying plate. The oceanic crust is assumed to thicken by a factor of 1.5 away from the ridge axis, and the thickness of the lithosphere (age is indicated in italics) was calculated following Parsons and McKenzie [1978] and Turcotte and Schubert [2002]. Note that the melting region is required to dip into the garnet peridotite zone on the basis of the large  $^{230}\text{Th}$  excesses observed [see also Sims *et al.*, 2002], and the location of the spinel to garnet transition is based on Robinson and Wood [1998]. In the second model, shown as the long-dashed curve, the length of the melting column additionally shortens away from the axis because it is also assumed that the effects of melt extraction in the central upwelling region results in cooler, more depleted peridotite moving away from the axis such that the depth of intersection with the solidus shallows (see text for details). This is inferred to result in a decreased clinopyroxene mode (assumed mineralogy is shown at the base of the illustration). Solid mantle flow lines are shown schematically in Figure 7a, and melt flow is assumed to be vertical. The location of the melt lens identified by Durant and Toomey [2009] and the Lamont seamounts on the Pacific plate are also shown. Samples plotted in Figure 7b are those inferred to have erupted off axis (cf. Figures 5 and 6) supplemented by the Lamont seamounts data from Lundstrom *et al.* [1999]. Ship not to scale.

**Table 4.** Input Parameters for Dynamic Melting Model

Parameter	Units		
Age (kyr) <sup>a</sup>	0–900		
Total melt extent X (%)	0.1		
Porosity $\phi$ (%)	0.001		
$\rho_s$ (kg/m <sup>3</sup> )	3300		
$\rho_f$ (kg/m <sup>3</sup> )	2800		
Melting column top (km) <sup>b</sup>	6–18		
Melting column bottom (km)	100–60		
Upwelling rate $W_s$ (cm/yr)	5.5		
Average pressure (Gpa)	1.5–2.2		
Partition Coefficients <sup>c</sup> and Mode	U	Th	Ra
Olivine (57%)	0.00006	9.52E-06	5.75E-08
Orthopyroxene (28–34%)	0.0030	0.0017	6.00E-07
Clinopyroxene (7–15%)	0.0119–0.0121	0.0101–0.0108	4.13E-06
Garnet (8–0%)	0.015	0.002	7.00E-09

<sup>a</sup>Calculated assuming a half-spreading rate of 5.5 cm/yr.

<sup>b</sup>Calculated assuming  $z_l = 2.32 \cdot \sqrt{(k \cdot t)}$  as discussed in the text.

<sup>c</sup>From Blundy and Wood [2003], Salters *et al.* [2002], and Adam and Green [2006]; clinopyroxene U-Th partitioning was calculated following Landwehr *et al.* [2001] for the average pressure of the melt columns.

recently been reviewed by Elliott and Spiegelman [2003] to which the reader is referred for a detailed discussion. Key parameters are the mineral melt partition coefficients [cf. Wood *et al.*, 1999; Landwehr *et al.*, 2001], the porosity of the melting region ( $\phi$ ), the length of the melt column and the melting rate ( $\Gamma$ ). The latter is linked to the upwelling rate ( $W_s$ ) that will, in turn, equate to the half-spreading rate directly beneath the ridge axis. Of these, it is decreasing melt column length (which reduces the time available for daughter ingrowth) that seems the most likely candidate to explain the off-axis decrease in initial ( $^{230}\text{Th}/^{238}\text{U}$ ) that we now explore further.

[34] A model illustrating the effects of decreasing melt column length, due to the thickening of the overlying plate, on U-Th disequilibria is illustrated in Figure 7a. The thickness of the lithosphere ( $z_l$ ) and increase in bathymetry away from the ridge axis is proportional to its age [e.g., Parsons and McKenzie, 1978; Turcotte and Schubert, 2002]:

$$z_l = 2.32 \cdot \sqrt{(k \cdot t)},$$

where  $k$  is the thermal conductivity,  $\sim 2^{-6} \text{ m}^2/\text{s}$  [Chai *et al.*, 1996], and  $t$  is time. Accordingly, the lithospheric thickness increases from near zero at the ridge axis to  $\sim 18 \text{ km}$  at age 800 kyr reducing the length of putative melt columns. In Figure 7b we show the results of a dynamic melting model, based on Williams and Gill [1989], to simulate this scenario. At the axis, the magnitude of measured  $^{230}\text{Th}$  excesses indicate that the axial melt region reaches into the garnet stability zone [cf. Sims

*et al.*, 2002] which is located at  $\sim 83 \text{ km}$ , based on the experiments of Robinson and Wood [1998]. The porosity was set at  $10^{-3}$  to achieve or exceed the minimum ( $^{226}\text{Ra}/^{230}\text{Th}$ ) ratios observed in the data (resultant model ( $^{226}\text{Ra}/^{230}\text{Th}$ ) values were 2.2–2.9). Other parameters are given in Table 4. Our calculations show that ( $^{230}\text{Th}/^{238}\text{U}$ ) is indeed predicted to decrease with increasing distance away from the ridge axis but that the effect is insufficient to simulate the data (Figure 7b).

[35] Depending on the geometry of the matrix flow lines, off-axis regions experience a decrease in the depth of the solidus as melt extraction leads to the source region becoming cooler and possibly more depleted or refractory [e.g., Reynolds and Langmuir, 2000]. The latter would likely result in an absence of garnet and decreasing clinopyroxene mode in the residue such that Th becomes less incompatible relative to U (see Figure 7a and Table 4). Thus, Figure 7b shows the results of a second model in which the depth of onset of melting shallows, and fertility decreases away from the axis (see Figure 7a). We assumed that the solidus for depleted peridotite occurs at  $\sim 2 \text{ GPa}$  at a temperature of  $\sim 1380^\circ\text{C}$  [Jaques and Green, 1980]. This model is highly simplistic but, nevertheless, provides a better simulation of the off-axis decrease in ( $^{230}\text{Th}/^{238}\text{U}$ ). Note that we kept the total melt fraction and the upwelling rate constant and it is important to recognize that the probable decrease in both of these away from the axis would lead to higher  $^{230}\text{Th}$  excesses that would worsen the approximation of the data. Clearly, even relatively modest changes in porosity, extent of



melting and partition coefficients would have significant effects on the results and one could envisage a family of models with broadly similar outcomes. However, fundamental limitations of the data set do not warrant more sophisticated calculations (equilibrium transport, two-porosity, etc.) that must await further constraints on the numerous input assumptions (e.g., more detailed sampling,  $^{231}\text{Pa}$  measurements to better constrain primary disequilibria, porosity etc). Mixing may also be important [e.g., *Sims et al.*, 2002].

## 7. Summary

[36] U-Th-Ra analyses of samples from traverses extending up to 50 km either side of the East Pacific Rise at 9°30N, 10°30N and 11°20N are consistent with the bulk of samples having formed in an axial region that is ~8 km wide. Although the large  $^{230}\text{Th}$  and  $^{238}\text{U}$  excesses reported by *Zou et al.* [2002] have not been substantiated we do find evidence for some anomalously young samples tens of kilometers from the axis. These are consistent with recent seismic interpretation of a magma lens at this distance, at least to the east of the ridge [Durant and Toomey, 2009].

[37] The samples inferred to have erupted off axis have low initial ( $^{230}\text{Th}/^{238}\text{U}$ ) compared to axial samples, both here and in other studies [e.g., *Sims et al.*, 2003; *Standish and Sims*, 2010]. There is little evidence that this reflects source heterogeneity. Decreasing melting column length and shallowing of the solidus could, in principle, explain the decreases in primary ( $^{230}\text{Th}/^{238}\text{U}$ ) ratios away from the ridge axis. The alternative, that the lower ( $^{230}\text{Th}/^{238}\text{U}$ ) ratios reflect aging, seems precluded by the  $^{226}\text{Ra}$  data whereas the formed interpretation is supported by the observed decrease in ( $^{230}\text{Th}/^{238}\text{U}$ ) across the Lamont seamounts to the west of the EPR axis.

[38] The most profound conclusion is that magma focusing beneath the ridge axis may not be as efficient as widely believed, despite the earlier recognition of active off-axis seamount volcanism [Batiza et al., 1990]. This may have significant implications for recent chromatographic melt migration models [e.g., *Spiegelman et al.*, 2001]. Future work should be aimed at increasing the spatial resolution of across-axis data, include additional seamount analyses and  $^{231}\text{Pa}$  measurements to further test the age implications and to constrain the porosity in the melt region.

## Acknowledgments

[39] We gratefully acknowledge the contribution of Rodey Batiza to the sampling program and thank Peter Wieland, Norman Pearson, John Caulfield, and Heather Handley for their help with the isotope analyses. Mike Perfit is thanked for useful discussions and for supplying the BBQ flow sample. Christoph Beier was supported by a Feodor Lynen fellowship of the Alexander von Humboldt Foundation and thanks Gutmann for inspiration. Simon Turner was supported by an Australian Research Council Federation Fellowship and worked on the data in Yelapa, Mexico, adjacent to the East Pacific Rise, for inspiration. We thank Ken Rubin, Julie Prytulak, an anonymous reviewer, and Associate Editor Dave Peate for comments that helped to improve the paper. This work was directly funded by ARC Discovery Proposal DP0771610 and used instrumentation funded by ARC LIEF and DEST Systemic Infrastructure Grants, Macquarie University and Industry. This is GEMOC publication 699.

## References

- Adam, J., and T. Green (2006), Trace element partitioning between mica- and amphibole-bearing garnet lherzolite and hydrous basanitic melt: 1. Experimental results and the investigation of controls on partitioning behaviour, *Contrib. Mineral. Petrol.*, **152**, 1–17, doi:10.1007/s00410-006-0085-4.
- Batiza, R., Y. Niu, and W. C. Zayac (1990), Chemistry of seamounts near the East Pacific Rise: Implications for the geometry of subaxial mantle flow, *Geology*, **18**, 1122–1125, doi:10.1130/0091-7613(1990)018<1122:COSENTE>2.3.CO;2.
- Batiza, R., Y. L. Niu, J. L. Karsten, W. Boger, E. Potts, and L. Norby (1996), Steady and non-steady state magma chambers below the East Pacific Rise, *Geophys. Res. Lett.*, **23**, 221–224.
- Beier, C., S. P. Turner, J. M. Sinton, and J. B. Gill (2010), Influence of subducted components on back-arc melting dynamics in the Manus Basin, *Geochem. Geophys. Geosyst.*, **11**, Q0AC03, doi:10.1029/2010GC003037.
- Birck, J. L. (1986), K, Rb, Sr isotopic analysis: Application to Rb-Sr chronology, *Chem. Geol.*, **56**, 73–83, doi:10.1016/0009-2541(86)90111-7.
- Blundy, J. D., and B. J. Wood (2003), Mineral-melt partitioning of uranium-thorium and their daughters, *Rev. Mineral. Geochem.*, **52**, 59–123, doi:10.2113/0520059.
- Chai, M., J. M. Brown, and L. J. Slutsky (1996), Thermal diffusivity of mantle minerals, *Phys. Chem. Miner.*, **23**, 470–475, doi:10.1007/BF00202033.
- Chen, J. H., R. L. Edwards, and G. J. Wasserburg (1986),  $^{238}\text{U}$ ,  $^{234}\text{U}$  and  $^{232}\text{Th}$  in seawater, *Earth Planet. Sci. Lett.*, **80**, 241–251, doi:10.1016/0012-821X(86)90108-1.
- Cheng, H., R. L. Edwards, J. Hoff, C. D. Gallup, D. A. Richards, and Y. Asmerom (2000), The half lives of uranium-234 and thorium-230, *Chem. Geol.*, **169**, 17–33, doi:10.1016/S0009-2541(99)00157-6.
- Christeson, G. L., G. M. Purdy, and G. J. Fryer (1992), Structure of young upper crust at the East Pacific Rise near 9°N, *Geophys. Res. Lett.*, **19**, 1045–1048, doi:10.1029/91GL00971.
- Davies, G. F. (2009), Reconciling the geophysical and geochemical mantles: Plume flows, heterogeneities and disequi-

- librium, *Geochem. Geophys. Geosyst.*, **10**, Q10008, doi:10.1029/2009GC002634.
- Durant, D. T., and D. R. Toomey (2009), Evidence and implications of crustal magmatism on the flanks of the East Pacific Rise, *Earth Planet. Sci. Lett.*, **287**, 130–136, doi:10.1016/j.epsl.2009.08.003.
- Elkins, L. J., G. A. Gaetani, and K. W. W. Sims (2008), Partitioning of U and Th during garnet pyroxenite partial melting: Constraints on the source of alkaline ocean island basalts, *Earth Planet. Sci. Lett.*, **265**, 270–286, doi:10.1016/j.epsl.2007.10.034.
- Elliott, T. (2002), Caught offside, *Science*, **295**, 55–57, doi:10.1126/science.1066318.
- Elliott, T., and M. Spiegelman (2003), Melt migration in oceanic crustal production: A U-series perspective, *Treatise Geochem.*, **3**, 465–510.
- Fornari, D. J., M. R. Perfit, J. F. Allan, and R. Batiza (1988), Small-scale heterogeneities in depleted mantle sources: Near-ridge seamount lava geochemistry and implications for mid-ocean ridge magmatic processes, *Nature*, **331**, 511–513, doi:10.1038/331511a0.
- Fornari, D. J., et al. (2004), Submarine lava flow emplacement at the East Pacific Rise 9°50'N: Implications for uppermost ocean crust stratigraphy and hydrothermal fluid circulation, *Geophys. Monogr.*, **148**, 187–217.
- Garman, J. (1989), Accumulations of melt at the base of young oceanic crust, *Nature*, **340**, 628–632, doi:10.1038/340628a0.
- Goldstein, S. J., M. T. Murrell, D. R. Janecky, J. R. Delaney, and D. A. Clague (1992), Erratum: Geochronology and petrogenesis of MORB from Juan de Fuca and Gorda ridges by <sup>238</sup>U–<sup>230</sup>Th disequilibrium, *Earth Planet. Sci. Lett.*, **109**, 255–272, doi:10.1016/0012-821X(92)90088-D.
- Goldstein, S. J., M. R. Perfit, R. Batiza, D. J. Fornari, and M. T. Murrell (1994), Off-axis volcanism at the East Pacific Rise detected by uranium-series dating of basalts, *Nature*, **367**, 157–159, doi:10.1038/367157a0.
- Harding, A. J., G. M. Kent, and J. A. Orcutt (1993), A multi-channel seismic investigation of upper crustal structure at 9°N on the East Pacific Rise: Implications for crustal accretion, *J. Geophys. Res.*, **98**, 13,925–13,944, doi:10.1029/93JB00886.
- Haymon, R. M., et al. (1993), Volcanic eruption of the mid-ocean ridge along the East Pacific Rise crest at 9°45'–52'N: Direct submersible observations of seafloor phenomena associated with an eruption event in April, 1991, *Earth Planet. Sci. Lett.*, **119**, 85–101, doi:10.1016/0012-821X(93)90008-W.
- Hoffmann, D. L., J. Prytulak, D. A. Richards, T. R. Elliott, C. D. Coath, P. L. Smart, and D. Scholz (2007), Procedures for accurate U and Th isotope measurements by high precision MC-ICPMS, *Int. J. Mass. Spectrom.*, **264**, 97–109, doi:10.1016/j.ijms.2007.03.020.
- Jaques, A. L., and D. H. Green (1980), Anhydrous melting of peridotite at 0–15 Kbar pressure and the genesis of tholeiitic basalts, *Contrib. Mineral. Petrol.*, **73**, 287–310, doi:10.1007/BF00381447.
- Jull, M., P. Kelemen, and K. W. W. Sims (2002), Consequences of diffuse and channeled porous melt migration on uranium series disequilibrium, *Geochim. Cosmochim. Acta*, **66**, 4133–4148, doi:10.1016/S0016-7037(02)00984-5.
- Kokfelt, T. F., C. Lundstrom, K. Hoernle, F. Hauff, and R. Werner (2005), Plume-ridge interaction studied at the Galapagos spreading center: Evidence from <sup>226</sup>Ra–<sup>230</sup>Th–<sup>238</sup>U and <sup>231</sup>Pa–<sup>235</sup>U isotopic disequilibria, *Earth Planet. Sci. Lett.*, **234**, 165–187, doi:10.1016/j.epsl.2005.02.031.
- Korenaga, J., and P. B. Kelemen (1997), The origin of gabbro sills in the mocho transition zone of the Oman ophiolite: Implications for magma transport in the oceanic lower crust, *J. Geophys. Res.*, **102**, 27,729–27,749, doi:10.1029/97JB02604.
- Landwehr, D., J. Blundy, E. M. Chamorro-Perez, E. Hill, and B. Wood (2001), U-series disequilibria generated by partial melting of spinel lherzolite, *Earth Planet. Sci. Lett.*, **188**, 329–348, doi:10.1016/S0012-821X(01)00328-4.
- Lundstrom, C. C., Q. Williams, and J. B. Gill (1998), Investigating solid mantle upwelling rates beneath mid-ocean ridges using U-series disequilibria, 1: A global approach, *Earth Planet. Sci. Lett.*, **157**, 151–165, doi:10.1016/S0012-821X(98)00038-7.
- Lundstrom, C. C., D. E. Sampson, M. R. Perfit, J. Gill, and Q. Williams (1999), Insights into mid-ocean ridge basalt petrogenesis: U-series disequilibria from the Siqueiros Transform, Lamont Seamounts, and East Pacific Rise, *J. Geophys. Res.*, **104**, 13,035–13,048, doi:10.1029/1999JB900081.
- Niu, Y. L., and R. Batiza (1997), Trace element evidence from seamounts for recycled oceanic crust in the eastern equatorial Pacific mantle, *Earth Planet. Sci. Lett.*, **148**, 471–483, doi:10.1016/S0012-821X(97)00048-4.
- Niu, Y., and M. O'Hara (2008), Global correlations of ocean ridge basalt chemistry with axial depth: A new perspective, *J. Petrol.*, **49**, 633–664, doi:10.1093/petrology/egm051.
- Niu, Y. L., G. Waggoner, J. M. Sinton, and J. J. Mahoney (1996), Mantle source heterogeneity and melting processes beneath seafloor spreading centers: The East Pacific Rise 18°–19°S, *J. Geophys. Res.*, **101**, 27,711–27,733, doi:10.1029/96JB01923.
- Niu, Y., K. D. Collerson, R. Batiza, J. L. Wendt, and M. Regelous (1999), Origin of enriched-type mid-ocean ridge basalt at ridges far from mantle plumes: The East Pacific Rise at 11°20'N, *J. Geophys. Res.*, **104**, 7067–7087, doi:10.1029/1998JB900037.
- O'Neill, H. S. C., and G. Mallmann (2007), The P/Nd ratio of basalt as an indicator of pyroxenite in its source, *Geochim. Cosmochim. Acta*, **71**, A741.
- Parsons, B., and D. McKenzie (1978), Mantle convection and the thermal structure of the plates, *J. Geophys. Res.*, **83**, 4485–4496, doi:10.1029/JB083iB09p04485.
- Perfit, M. R., and W. W. Chadwick Jr. (1998), Magmatism at mid-ocean ridges: Constraints from volcanological and geochemical investigations, in *Faulting and Magmatism at Mid-Ocean Ridges*, *Geophys. Monogr. Ser.*, vol. 106, edited by W. R. Buck, pp. 59–116, AGU, Washington, D. C.
- Perfit, M. R., D. J. Fornari, M. C. Smith, J. F. Bender, C. H. Langmuir, and R. M. Haymon (1994), Small-scale spatial and temporal variations in mid-ocean ridge crest magmatic processes, *Geology*, **22**, 375–379, doi:10.1130/0091-7613(1994)022<0375:SSSATV>2.3.CO;2.
- Petermann, M., and M. M. Hirschmann (2003), Partial melting experiments on a MORB-like pyroxenite between 2 and 3 GPa: Constraints on the presence of pyroxenite in basalt source regions from solidus location and melting rate, *J. Geophys. Res.*, **108**(B2), 2125, doi:10.1029/2000JB000118.
- Plank, T., and C. H. Langmuir (1992), Effects of the melting regime on the composition of the oceanic crust, *J. Geophys. Res.*, **97**, 19,749–19,770, doi:10.1029/92JB01769.
- Prytulak, J., and T. Elliott (2009), Determining melt productivity of mantle sources from <sup>238</sup>U–<sup>230</sup>Th and <sup>235</sup>U–<sup>231</sup>Pa disequilibria: An example from Pico Island, Azores, *Geochim. Cosmochim. Acta*, **73**, 2103–2122, doi:10.1016/j.gca.2009.01.001.



- Regelous, M., Y. Niu, J. I. Wendt, R. Batiza, A. Greig, and K. D. Collerson (1999), Variations in the geochemistry of magmatism on the East Pacific Rise at 10°30'N since 800 ka, *Earth Planet. Sci. Lett.*, *168*, 45–63, doi:10.1016/S0012-821X(99)00048-5.
- Reynolds, J. R., and C. H. Langmuir (2000), Identification and implications of off-axis lava flows around the East Pacific Rise, *Geochem. Geophys. Geosyst.*, *1*, 1019, doi:10.1029/1999GC000033.
- Robinson, J. A. C., and B. J. Wood (1998), The depth of the spinel to garnet transition at the peridotite solidus, *Earth Planet. Sci. Lett.*, *164*, 277–284, doi:10.1016/S0012-821X(98)00213-1.
- Rubin, K. H., J. D. Macdougall, and M. R. Perfit (1994), <sup>210</sup>Po–<sup>210</sup>Pb dating of recent volcanic eruptions on the sea floor, *Nature*, *368*, 841–844, doi:10.1038/368841a0.
- Rubin, K. H., I. van der Zander, M. C. Smith, and E. C. Bergmanis (2005), New speed limit for ocean ridge magmatism, *Nature*, *437*, 534–538, doi:10.1038/nature03993.
- Russo, C. J., K. H. Rubin, and D. W. Graham (2009), Mantle melting and magma supply to the southeast Indian ridge: The roles of lithology and melting conditions from U-series disequilibria, *Earth Planet. Sci. Lett.*, *278*, 55–66, doi:10.1016/j.epsl.2008.11.016.
- Saal, A. E., and J. A. Van Orman (2004), The <sup>226</sup>Ra enrichment in oceanic basalts: Evidence for melt-cumulate diffusive interaction processes within the oceanic lithosphere, *Geochem. Geophys. Geosyst.*, *5*, Q02008, doi:10.1029/2003GC000620.
- Salters, V., J. Longhi, and M. Bizimis (2002), Near mantle solidus trace element partitioning at pressures up to 3.4 GPa, *Geochem. Geophys. Geosyst.*, *3*(7), 1038, doi:10.1029/2001GC000148.
- Sims, K. W. W., et al. (2002), Chemical and isotopic constraints on the generation and transport of magma beneath the East Pacific Rise, *Geochim. Cosmochim. Acta*, *66*, 3481–3504, doi:10.1016/S0016-7037(02)00909-2.
- Sims, K. W. W., et al. (2003), Aberrant youth: Chemical and isotopic constraints on the origin of off-axis lavas from the East Pacific Rise, 9°–10°N, *Geochem. Geophys. Geosyst.*, *4*(10), 8621, doi:10.1029/2002GC000443.
- Sims, K. W. W., et al. (2008), An inter-laboratory assessment of the Th isotopic composition of synthetic and rock standards, *Geostand. Geoanal. Res.*, *32*, 65–91, doi:10.1111/j.1751-908X.2008.00870.x.
- Sinton, J. M., and R. S. Detrick (1992), Mid-ocean ridge magma chambers, *J. Geophys. Res.*, *97*, 197–216, doi:10.1029/91JB02508.
- Sobolev, A. V., et al. (2007), Estimating the amount of recycled crust in sources of mantle-derived melts, *Science*, *316*, 412–417, doi:10.1126/science.1138113.
- Sohn, R. A., and K. W. W. Sims (2005), Bending as a mechanism for triggering off-axis volcanism on the East Pacific Rise, *Geology*, *33*, 93–96, doi:10.1130/G21116.1.
- Sohn, R. A., S. C. Webb, and J. A. Hildebrand (2004), Fine-scale seismic structure of the shallow volcanic crust on the East Pacific Rise at 9°50'N, *J. Geophys. Res.*, *109*, B12104, doi:10.1029/2004JB003152.
- Soule, S. A., D. J. Fornari, M. R. Perfit, M. A. Tivey, W. I. Ridley, and H. Schouten (2005), Channelized lava flows at the East Pacific Rise crest 9°–10°N: The importance of off-axis lava transport in developing the architecture of young oceanic crust, *Geochem. Geophys. Geosyst.*, *6*, Q08005, doi:10.1029/2005GC000912.
- Soule, S. A., D. J. Fornari, M. R. Perfit, and K. H. Rubin (2007), New insights into mid-ocean ridge volcanic processes from the 2005–2006 eruption of the East Pacific Rise, 9°46'N–9°56'N, *Geology*, *35*, 1079–1082, doi:10.1130/G23924A.1.
- Spiegelman, M., and D. McKenzie (1987), Simple 2-D models for melt extraction at mid-ocean ridges and island arcs, *Earth Planet. Sci. Lett.*, *83*, 137–152, doi:10.1016/0012-821X(87)90057-4.
- Spiegelman, M., P. B. Kelemen, and E. Aharonov (2001), Causes and consequences of flow organization during melt transport: The reaction infiltration instability in compactable media, *J. Geophys. Res.*, *106*, 2061–2077, doi:10.1029/2000JB900240.
- Standish, J. J., and K. W. W. Sims (2010), Young off-axis volcanism along the ultra-slow-spreading Southwest Indian Ridge, *Nat. Geosci.*, *3*, 286–292, doi:10.1038/ngeo824.
- Turcotte, D. L., and G. Schubert (2002), *Geodynamics*, 456 pp., Cambridge Univ. Press, Cambridge, U. K.
- Turner, S., B. Bourdon, C. Hawkesworth, and P. Evans (2000), <sup>226</sup>Ra–<sup>230</sup>Th evidence for multiple dehydration events, rapid melt ascent and the time scales of differentiation beneath the Tonga-Kermadec island arc, *Earth Planet. Sci. Lett.*, *179*, 581–593, doi:10.1016/S0012-821X(00)00141-2.
- Wessel, P., and W. H. F. Smith (1991), Free software helps map and display data, *Eos Trans. AGU*, *72*(41), 441, doi:10.1029/90EO00319.
- Wessel, P., and W. H. F. Smith (1998), New, improved version of the Generic Mapping Tools released, *Eos Trans. AGU*, *79*(47), 579, doi:10.1029/98EO00426.
- Williams, R. W., and J. B. Gill (1989), Effects of partial melting on the uranium decay series, *Geochim. Cosmochim. Acta*, *53*, 1607–1619, doi:10.1016/0016-7037(89)90242-1.
- Wood, B. J., J. D. Blundy, and J. A. C. Robinson (1999), The role of clinopyroxene in generating U-series disequilibria during mantle melting, *Geochim. Cosmochim. Acta*, *63*, 1613–1620, doi:10.1016/S0016-7037(98)00302-0.
- Zou, H., A. Zindler, and Y. Niu (2002), Constraints on melt movement beneath the East Pacific Rise from <sup>230</sup>Th–<sup>238</sup>U disequilibrium, *Science*, *295*, 107–110, doi:10.1126/science.1064295.